PHYSICAL REVIEW B **92**, 125147 (2015)

Low-loss electron energy loss spectroscopy: An atomic-resolution complement to optical spectroscopies and application to graphene

Myron D. Kapetanakis,[1,2] Wu Zhou,[2] Mark P. Oxley,[1,2] Jaekwang Lee,[3] Micah P. Prange,[4] Stephen J. Pennycook,[5]
Juan Carlos Idrobo,[6] and Sokrates T. Pantelides[1,2]

[1]*Department of Physics and Astronomy, Vanderbilt University, Nashville, Tennessee 37235, USA*
[2]*Materials Science and Technology Division, Oak Ridge National Laboratory, Oak Ridge, Tennessee 37831, USA*
[3]*Department of Physics, Pusan National University, Busan 609-735, Korea*
[4]*Fundamental and Computational Sciences Directorate, Pacific Northwest National Laboratory, Richland, Washington 99352, USA*
[5]*Department of Materials Science and Engineering, National University of Singapore, Singapore 117576 Singapore*
[6]*Center for Nanophase Materials Sciences, Oak Ridge National Laboratory, Oak Ridge, Tennessee 37831, USA*

(Received 12 July 2015; published 25 September 2015)

Photon-based spectroscopies have played a central role in exploring the electronic properties of crystalline solids and thin films. Though they remain a powerful tool for probing the electronic properties of nanostructures, they are limited by lack of spatial resolution. On the other hand, electron-based spectroscopies, e.g., electron energy loss spectroscopy (EELS), are now capable of subangstrom spatial resolution. Core-loss EELS, a spatially resolved analog of x-ray absorption, has been used extensively in the study of inhomogeneous complex systems. In this paper, we demonstrate that low-loss EELS in an aberration-corrected scanning transmission electron microscope, which probes low-energy excitations, combined with a theoretical framework for simulating and analyzing the spectra, is a powerful tool to probe low-energy electron excitations with atomic-scale resolution. The theoretical component of the method combines density functional theory–based calculations of the excitations with dynamical scattering theory for the electron beam. We apply the method to monolayer graphene in order to demonstrate that atomic-scale contrast is inherent in low-loss EELS even in a perfectly periodic structure. The method is a complement to optical spectroscopy as it probes transitions entailing momentum transfer. The theoretical analysis identifies the spatial and orbital origins of excitations, holding the promise of ultimately becoming a powerful probe of the structure and electronic properties of individual point and extended defects in both crystals and inhomogeneous complex nanostructures. The method can be extended to probe magnetic and vibrational properties with atomic resolution.

DOI: 10.1103/PhysRevB.92.125147 PACS number(s): 68.37.Ma, 61.05.J−, 71.15.Mb, 79.20.Uv

I. INTRODUCTION

Optical spectroscopies along with energy-band theory were the cornerstones upon which modern solid-state physics was founded. Ultraviolet photoemission spectroscopy (UPS) and x-ray photoemission spectroscopy (XPS) were subsequently instrumental in the field of surface science. X-ray emission spectra (XES) and x-ray absorption spectra (XAS) and their many variants, e.g., resonant x-ray scattering, have also played significant roles in probing the electronic properties of solids. Infrared absorption has been a powerful probe of phonons and low-energy electronic excitations. The spatial resolution of these spectroscopies, however, is quite limited by the respective photon wavelengths and other factors [1,2]. Nevertheless, they continue to make major contributions in the study of nanostructures.

Electron-based spectroscopies have the advantage of ultrasmall de Broglie wavelengths, which enable high spatial resolution. Scanning transmission electron microscopes (STEMs) employ a highly focused electron beam, which produces direct images of crystalline films with atomic resolution. The primary imaging mode of the STEM is Z-contrast imaging, which relies on high-angle Rutherford scattering by atomic nuclei [3]. The intensity of scattered electrons is proportional to approximately the square of the atomic number Z. In addition, inelastic scattering of the focused beam yields spatially resolved electron energy loss spectra (EELS). The advent of aberration-corrected (S)TEMs has led to significantly enhanced spatial resolution [4–7] and ushered the era of "core-loss" EELS (electron excitations from core levels, analogs of XAS) with atomic resolution, especially at lower accelerating voltages [8–11]. These spectra enable the construction of "chemical maps" by plotting the integrated EELS of a characteristic edge of individual atomic species (e.g., an oxygen map constructed by plotting the integral over $10-20$ eV of the oxygen K edge) [12–15]. Similarly, maps of individual features of near-edge structure, e.g., the height or integral of a peak or the separation between two peaks, can be constructed [10,16]. It was recently demonstrated that such maps can be simulated by using a combination of density functional theory (DFT) to describe core-electron excitations and dynamical scattering theory to describe the evolution of the STEM's focused electron beam in the sample, including interference effects and the collection of the scattered electrons in the detector [6,11,17]. These simulations enable detailed analysis of the origins of excitations that give rise to individual spectral features and their variations as a function of the local environment.

In addition to the core-loss EELS, so-called "low-loss" EELS arises from low-energy excitations, typically valence-electron excitations (valence-electron energy loss spectra or VEELS). These are the analogs of optical and infrared absorption spectra. The key difference is that, in a perfect crystal, optical and infrared absorption arises from "direct" transitions in the Brillouin zone as low-energy photons carry negligible momentum. In contrast, VEELS in a perfect crystal arises from transitions with nonzero momentum transfer. In this sense, VEELS is a complement to optical and infrared spectroscopies. Published VEELS maps often exhibit features arising from defects [18] and interfaces [19,20]. Previous theoretical work has focused on plasmon excitations under plane-wave illumination [21,22]. Atomically resolved maps can also be obtained due to localization of phonon excitations [23]. Even in a perfect crystal, however, Bloch functions have spatial variations, whereby the question arises whether the spatial variation of valence-electron excitations can be captured by suitable VEELS maps. Extrapolation of arguments based on core-loss EELS has led to inferences that VEELS in perfect crystals is unlikely to yield sufficient contrast at different positions of the focused beam to generate atomic-resolution spatial maps [24–26].

In this paper, we report experimental VEELS data in pristine monolayer graphene that demonstate the existence of atomic-scale contrast. We also report the development of a corresponding theory and computer codes, based on DFT and dynamical scattering theory, that yield simulations of VEELS maps, enabling a detailed analysis of the transitions that underlie the spectra. This initial application to a perfect crystal establishes low-loss EELS as a powerful atomic-resolution complement of optical and infrared spectroscopies. Defects and interfaces naturally induce wave function localization, whereby the corresponding low-loss EELS has the potential of a powerful probe of electronic properties of defects in crystals and of nanostructures with atomic resolution. Data are still lacking, but the advent of new monochromators that give high-energy resolution and possible new solid-state detectors with higher signal-to-noise ratio promise that such data will be forthcoming. The methodologies and analysis presented here are uniquely suited for such data. For example, one can anticipate VEELS maps that provide characteristic signatures of defects with more than one stable configuration, can detect interdiffusion at interfaces, and many other applications. Ultimately, the present method can be extended to magnetism, as in electron magnetic chiral dichroism, and to phonons.

The rest of this paper is organized as follows: In Sec. II, we present the experimental technique and conditions under which the STEM-EELS experiments were performed and discuss the data obtained on a monolayer of pristine graphene. In Sec. III we introduce the theoretical framework of our method that allows us to simulate the experiment and directly compare with the data. In Sec. IV we discuss in detail the theoretical results and we sumarize our findings in Sec. V. Some further details regarding the theoretical simulations are discussed in the Appendixes.

II. EXPERIMENTAL DATA

The STEM-EELS experiments were performed with a Nion UltraSTEM, equipped with a cold-field emission electron source and a corrector of third- and fifth-order aberrations, operating at 60 kV accelerating voltage. After aberration correction, this microscope is capable of providing 1.065 Å information transfer limit in Z-contrast imaging, with a probe current of ∼110 pA. EEL spectra were collected using a Gatan Enfina spectrometer, with an energy resolution of 0.5 eV for 0.1 eV/channel energy dispersion. The convergence semiangle for the incident probe was ∼30 mrad, with an EELS collection semiangle of ∼48 mrad. Under these conditions we obtain that the maximum momentum transfer occurring in the experiment

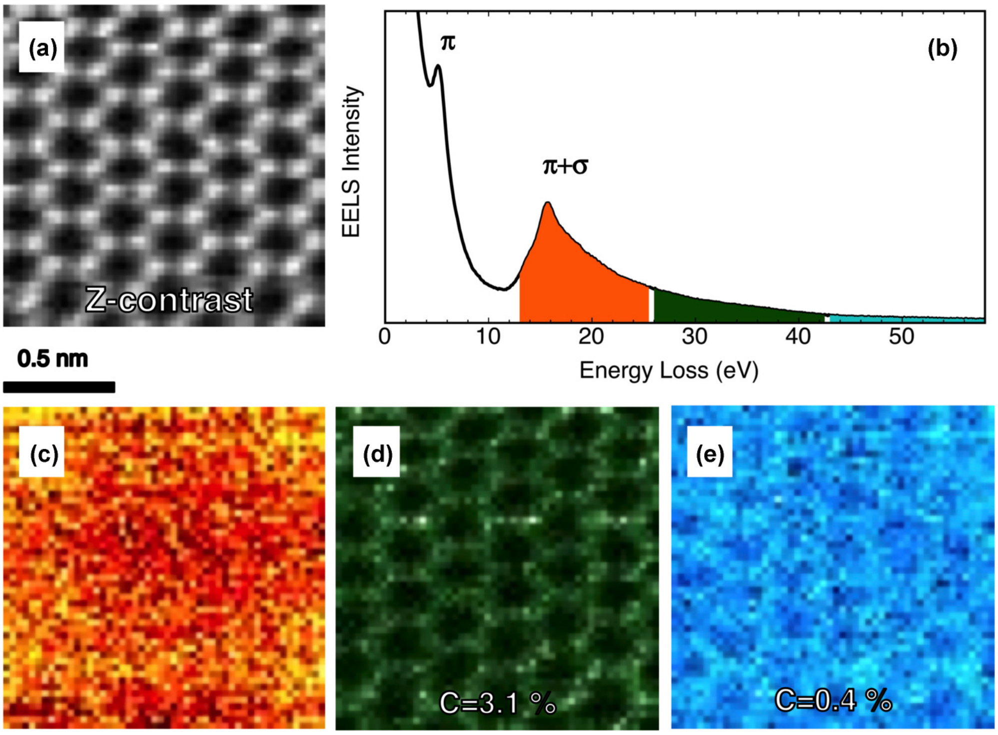

FIG. 1. (Color online) Simultaneously acquired Z-contrast image (a) and averaged VEEL spectrum (b). (c–e) VEEL spectrum images within the three energy loss windows highlighted in (b). (c) $13-26$ eV, (d) $26-42$ eV, (e) $42-58$ eV. The contrast is calculated by comparing the maximum (that occurs at the atomic positions) with the minimum value at the center of the hexagon.

is about 6 Å^{-1}, which is large enough to trigger excitations through the whole Brillouin zone. In order to increase the signal-to-noise ratio and avoid nonlocality effects, the majority of scattered electrons are collected. For the results shown in this manuscript, EEL spectrum images were collected from 0.5 to 134.5 eV energy loss range with 0.1 eV/channel dispersion, 0.02 s/pixel dwell time, and 0.257 Å pixel size. Z-contrast images were collected from ~86 to 200 mrad half-angle range. The VEEL spectrum images were obtained by plotting the VEELS intensity integrated in different energy loss ranges from the raw data, without any background subtraction or filtering, as a function of probe position.

Figure 1(a) shows a STEM Z-contrast image of monolayer graphene that was simultaneously acquired with a VEEL spectrum image. Figure 1(b) shows the averaged VEEL spectrum, which displays two main features, namely, the π and $\pi + \sigma$ peaks at 4.5 and 15 eV, respectively. We mapped out the spatial distribution of electronic excitations by integrating the intensity at the three different energy loss regions that are highlighted in Fig. 1(b).

The image in Fig. 1(e) obtained by integrating the spectra in the $13 - 26$ eV range does not show any atomic resolution or contrast, in apparent accord with the common belief that VEEL signals are delocalized [24–26]. Strikingly, the VEEL spectral image obtained within the intermediate energy range of $26 - 42$ eV, Fig. 1(d), displays a spatial resolution similar to the one observed in the Z-contrast image. We provide a quantitative assessment of the experimental images by defining the contrast using the formula $C = (I_{\text{MAX}} - I_{\text{MIN}})/I_{\text{MAX}}$ where I_{MAX} and I_{MIN} are maximum and minimum intensities in the image. This gives us a value of 3.1% for the contrast. In Fig. 1(e), although the image is noisier due to the lower intensity in this energy range, we are able to measure a weak atomic contrast of about 0.4% by excluding the noisiest areas of the image.

These results are not simply preservation of elastic image contrast [27], as seen in Ref. [28], since no contrast is observed in the integrated zero-loss peak (ZLP) image and the bright-field image shows reverse contrast as shown in Fig. 2. Figures 2(a) and 2(b) present the simultaneously acquired STEM-HAADF (high-angle annular-dark-field) image and the ZLP spectrum image in the energy range of -0.4 to 0.8 eV. While the HAADF image is noisy due to the limited number of pixels and short acquisition time, the graphene lattice can still be observed. Since the image in Fig. 2(b) is formed by an incoherent sum of elastically scattered electrons over a large detector collection angle, it shows no discernible coherent phase contrast. This should be compared to the weak inverse contrast exhibited by the conventional bright-field image shown in Fig. 2(d), which was simultaneously acquired with the HAADF image in Fig. 2(c). If the results shown in Fig. 1(d) were simply preservation of elastic image contrast, a similar level of image contrast should also be observed in the

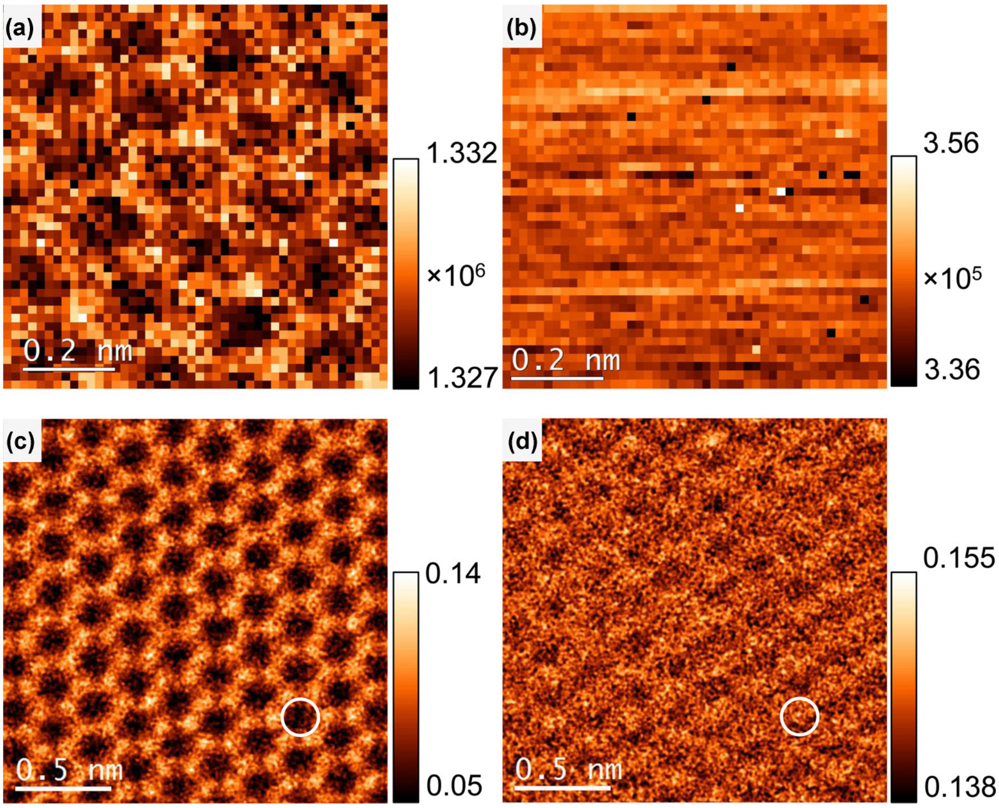

FIG. 2. (Color online) Zero-loss peak (ZLP) spectrum image and bright-field image from graphene. (a, b) Simultaneously acquired STEM-HAADF image (a) and ZLP spectrum image in the energy range of -0.4 to 0.8 eV (b). No obvious atomic contrast can be seen in the ZLP image. (c, d) Simultaneously acquired HAADF image (c) and BF image (d) at optimum focus for the HAADF image. These two images have been low-pass filtered in order to reduce the random noise. The white circles in the two images mark the identical positions. The carbon atoms display weak dark contrast in the BF image under this particular focus setting. The four images were acquired using different detectors and imaging conditions. The intensity is displayed in arbitrary units.

ZLP image. In contrast, the ZLP spectrum image is dominated by the noise from the electron source and shows no lattice information.

These results thus confirm that preservation of elastic image contrast is not the mechanism for the lattice contrast observed in our experimental VEELS image and that the spatial resolution of VEELS imaging can reach even the atomic level. We also performed STEM-VEEL spectrum imaging with different EELS collection semiangles (35 mrad), different energy dispersions (0.05 eV/channel,0.3 eV/channel), different energy loss collection onsets; atomic-resolution VEEL spectrum images were consistently obtained as those shown in Fig. 1.

III. THEORETICAL SIMULATIONS: INELASTIC IMAGE FORMATION BASED ON VALENCE-ELECTRON EXCITATIONS

The conditions under which atomic resolution is possible cannot be revealed by the experiment solely, but require a theoretical approach that takes into account the band structure effects in combination with the interactions with the fast electrons of the probe. The transition induced by the fast electron between different electronic states within a crystal is moderated by the Coulomb interaction and the real-space transition matrix element hence has the form

$$H_{n0}(\mathbf{r}) = \frac{e^2}{4\pi\varepsilon_0}\int \Psi_n^*(\mathbf{r}')\frac{1}{|\mathbf{r}-\mathbf{r}'|}\Psi_0(\mathbf{r}')d\mathbf{r}', \tag{1}$$

where $\mathbf{r}$ is the coordinate of the fast electron and $\mathbf{r}'$ the crystal coordinate. Here e is the electron charge and ε_0 the permittivity of free space. Also Ψ_n and Ψ_0 are the electronic crystal wave function for the states n and 0 with eigenvalues E_n and E_0 respectively. Equation (1) can be seen as a convolution of the probe intensity with the long-range Coulomb interaction, which introduces the delocalization of the excitation. For transmission electron microscopy it is usual to work in the projected potential approximation [29,30]. Writing $\mathbf{r} = (\mathbf{R},z)$ we define

$$H_{n0}(\mathbf{R}) = \int_0^t H_{n0}(\mathbf{r})e^{2\pi i q_z z}dz, \tag{2}$$

where q_z is the momentum transfer to the crystal along the beam (z) direction determined by the energy loss $E_{\mathrm{Loss}} = E_n - E_0$ and the incident energy E_0 by the formula $q_z \simeq k_0 E_{\mathrm{Loss}}/2E_0$ and t the crystal thickness. In order to calculate the inelastic image for the transition from the ground state 0 to the excited state n we need to construct the inelastic potential for this particular transition [30],

$$V_{n0}(\mathbf{R},E_{\mathrm{Loss}}) = \frac{\pi m_e}{h^2 k_n t}|H_{n0}(\mathbf{R})|^2\delta(E_{\mathrm{Loss}} - E_0 + E_n), \tag{3}$$

where E_{Loss} is the energy loss of the fast electron and m_e the mass of the electron. t is an effective thickness of the graphene layer, which drops out in the final equation for the measured spectral intensity (see below). For a single sheet of graphene we may neglect channeling of the fast electron and write the image formed by this particular transition as a convolution with the probe intensity [31–33],

$$I_{n0}(\mathbf{R}_0,E_{\mathrm{Loss}}) = \frac{4\pi}{h\upsilon}\int_0^t |P(\mathbf{R}_0,\mathbf{R},z)|^2 dz \otimes V_{n0}(\mathbf{R},E_{\mathrm{Loss}}). \tag{4}$$

Here υ is the velocity of the fast electron, $\mathbf{R}_0$ is the probe position, and $P(\mathbf{R}_0,\mathbf{R},z)$ the probe wave function (see Appendix Afor more details). Over the effective range of the projected potential the probe intensity may be considered to be approximately constant in the z direction. In this way Eq. (4) can be written as

$$I_{n0}(\mathbf{R}_0,E_{\mathrm{Loss}}) \simeq \frac{4\pi t}{h\upsilon}|P(\mathbf{R}_0,\mathbf{R})|^2 \otimes V_{n0}(\mathbf{R},E_{\mathrm{Loss}}). \tag{5}$$

Considering Eqs. (3) and (5), we conclude that the image intensity is independent of the crystal thickness, since the t factor in Eq. (5) cancels the $1/t$ factor in Eq. (3), which is an arbitrary constant for a two-dimensional system within the projected potential approximation. The only restriction about the thickness comes from the need to obtain fully converged electronic wave functions as discussed in Appendix C. The inelastic image is then determined by a linear combination of transitions that lie within a given energy range. For computational reasons it is more practical to calculate the transition matrix elements in reciprocal instead of real space as in Eqs. (2) and (3). The projected transition matrix element is given by the formula

$$H_{n0}(\mathbf{q}_\perp) = \frac{e^2}{4\pi\varepsilon_0}\left.\frac{\langle\Psi_n(\mathbf{r})|e^{-2\pi i\mathbf{q}\cdot\mathbf{r}}|\Psi_0(\mathbf{r})\rangle}{\mathbf{q}^2}\right|_{q_z}, \tag{6}$$

as a function of the transverse momentum transfer $\mathbf{q}_\perp$ and for fixed $\mathbf{q}_z$. The momentum transfer $\mathbf{q}$ is connected with the wave vectors $\mathbf{k}$ and $\mathbf{k}'$ of the fast electron before and after the inelastic scattering by the formula $h\mathbf{q} = h(\mathbf{k} - \mathbf{k}')$. Note that the delocalization of the VEEL excitation is expressed by the term $1/\mathbf{q}^2$ in Eq. (6). The real-space transition matrix element is then calculated via an inverse Fourier transform of the reciprocal space matrix element. The transition matrix element in Eq. (6) is calculated within the formalism of the projector augmented wave method (PAW) method and is further discussed in Appendix B.

We have, therefore, developed a theoretical scheme that allows us to simulate the images that are formed by valence-electron excitations. Within the framework of this theory we are able to study VEELS through the low-loss energy range—up to 50eV above the Fermi level—on an equal footing. Our method allows us to calculate images within a given energy range or between particular electronic states without invoking the dipole approximation. The latter is essential for a realistic simulation of STEM-VEELS experiments where a nonvanishing amount of momentum transfer is always present. Within this scheme, such images are essentially equivalent to the inelastic scattering cross section that describes the excitations of valence electrons through inelastic scattering by the fast electrons of the microscope probe.

With the theoretical method described here we can provide a direct simulation of the experimental results of Fig. 1. Figure 3(a) shows the calculated Z-contrast image, which displays the hexagonal structure of graphene. Figure 3(b) shows the

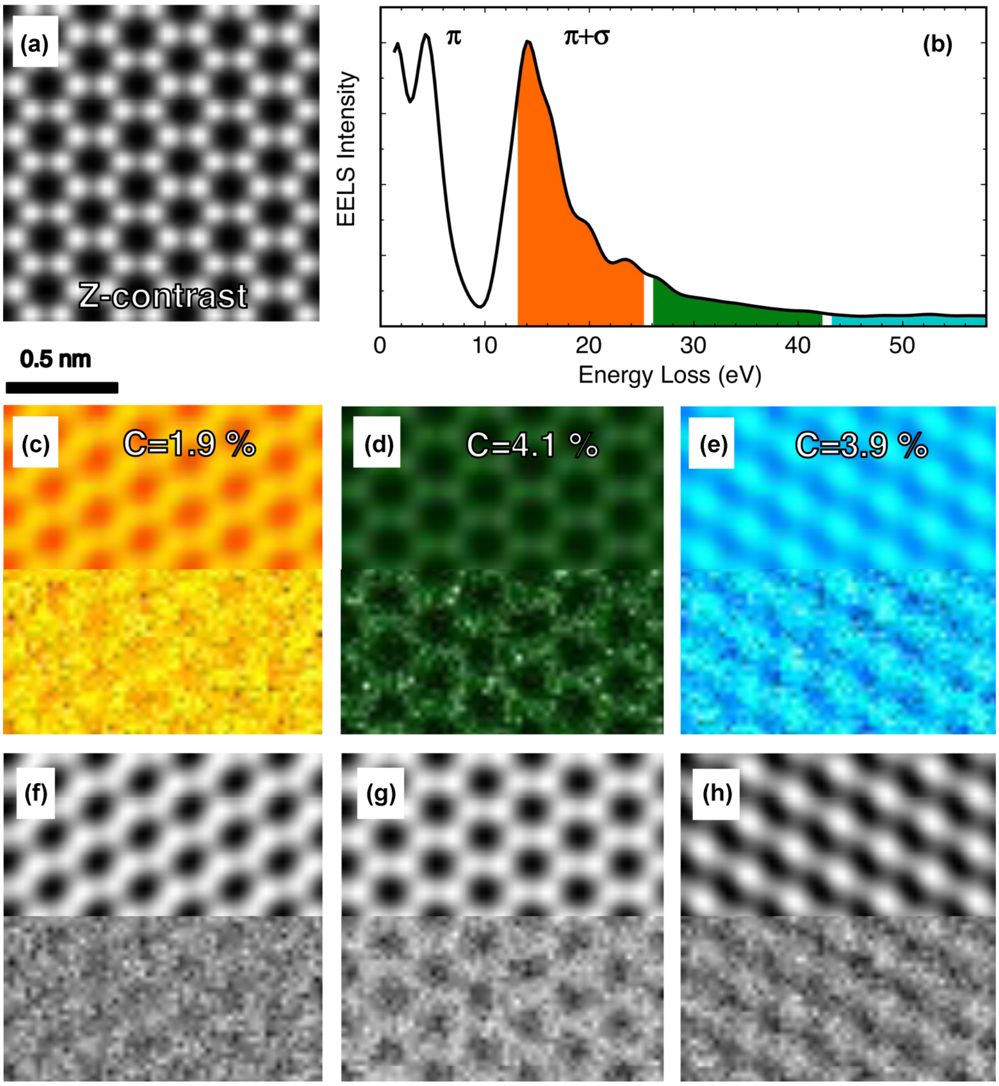

FIG. 3. (Color online) Calculated Z-contrast image (a) and VEEL spectrum (b). (c–e) Integrated spectroscopic images obtained with the same energy windows as in Fig. 1 without (upper halves) and with the addition of noise (lower halves). Panels (f–h) are the gray-scaled versions of (c–e), correspondingly. To visually emphasize the contrast variations panels (c–e) have been normalized to a common mean and displayed over a common intensity range.

calculated area-averaged VEEL spectrum. We see that the theoretical result is in good agreement with the experimental data. The two main calculated graphene peaks are located at about the same energies as in the experimental data with a slight shift of about 1 eV toward lower energies. The latter is due to excitonic effects [34], which were neglected in the calculations.

We continue now with the calculation of VEELS images by applying Eq. (5) and integrating over the same energy ranges as in Fig. 1. Within the intermediate energy range the image displays the hexagonal symmetry of pristine graphene with a contrast about 4.1%, which is consistent with the experimentally obtained value of 3.9% as shown in Fig. 1(d). We obtain a low contrast about 1.9% for the low-energy region—Fig. 3(c)—whereas for the higher energies it increases to 3.9% but without showing a graphenelike structure. Note that noise is always present is such experiments making the observation of weak contrast rather difficult. The latter is demonstrated in the lower halves of Figs. 3(c)–3(e) where a certain level of noise with a standard deviation of 1% is added to the simulated images. In this way any contrast disappears in Fig. 3(c) while the graphenelike structure in Fig. 3(d) remains intact. To further compare the experiment with the theoretical results in a more quantitative way we consider the line profile measurements. In Fig. 4 we show the line profile of the experimental VEELS image of Fig. 1(d) and the corresponding ones of the simulation derived by the images in Figs. 3(c)–3(e). The measurements are taken along a line shown in Fig. 4(b). We observe that the maximum intensity within the energy range of $26-42$ eV for both experiment and simulation coincides with the positions of the carbon atoms, while the minimum intensity occurs at the center of the hexagonal rings. On the other hand the line profiles for the lower or the higher energy diverge from a graphenelike profile as we clearly see in Figs. 3(c) and 3(e). We conclude that our theoretical technique provides a realistic description of VEELS excitations, which is in accordance with the STEM-EELS

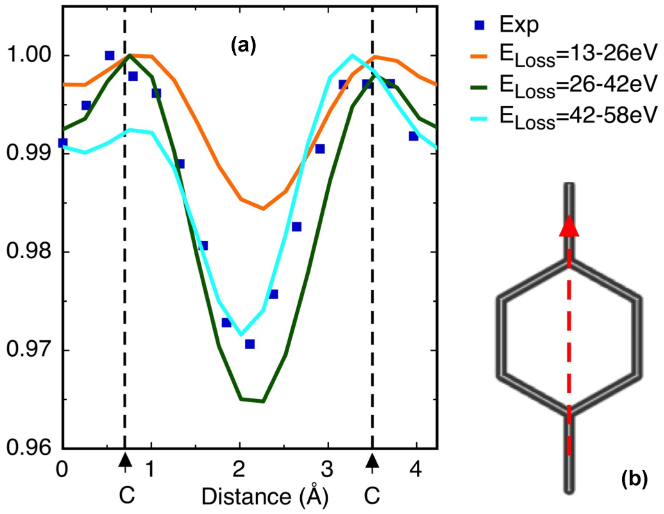

FIG. 4. (Color online) (a) Line profile measurements for the experimental image in Fig. 1(d) (blue squares) and the theoretical images in Figs. 3(c)–3(e) (solid lines). In order to account for the experimental noise the experimental profile is taken within the less noisy area of the image in Fig. 1(d). (b) A sketch showing the line along which the measurements are taken. The two dashed lines in (a) show the positions of the carbon atoms. Measurements are normalized to show the variations with respect to the energy.

experiments and therefore can be used to further study the nature of the experimental results. The latter is the focus of the rest of this paper.

IV. DISCUSSION

The theoretical technique discussed in Sec. III allows us to examine the contribution of each transition separately as a function of electron probe position, and so identify the origin of the experimentally observed contrast. In order to identify the character of a particular VEELS excitation one needs to study the character of the underlying states. The degree of atomic character is determined by the projection of the electronic Bloch wave functions onto a spherical harmonic centered on a particular atomic position. The latter is defined by the formula $P_{nlmk} = \langle Y_{lm} \mid \Psi_{nk} \rangle$ by integrating within a sphere around a particular atomic position. That quantity becomes large when the overlap between the states involved increases, and therefore provides a qualitative criterion of the atomic character of the electronic wave function. This analysis reveals the complex character of the band structure of pristine graphene. As shown in Fig. 5, the graphene conduction band consists of isolated "islands" of states where the atomic character is high in comparison with the surrounding states. These states can be identified as having s, p_z, p_{xy}, or d character, reflecting the existence of sp^2 hybridization in the hexagonal graphene.

In Fig. 6 we focus on excitations at the Γ point in the Brillouin zone (BZ)—where the atomic character of the states is highest—and show images from excitations between states with maximum atomic character. In this way, we demonstrate the character of a VEELS image with respect to the character of the underlying exitations. Such images reflect the symmetries of the involved states, for example, p_x or p_y orbitals on each atom, which may differ from the hexagonal symmetries of graphene. Figures 6(a)–6(c) show calculated images from the non-dipole-allowed s to s, p_z to p_z, and p_{xy} to p_{xy} excitations, correspondingly. We observe that all three images exhibit a graphenelike structure with a very high contrast and therefore contribute the most to the total VEEL image contrast. Figure 6(d) shows the spectrum image of a dipole-allowed transition that also exhibits atomic character. The images due to p_z to d transitions in Fig. 6(e) show strong atomic contrast, but

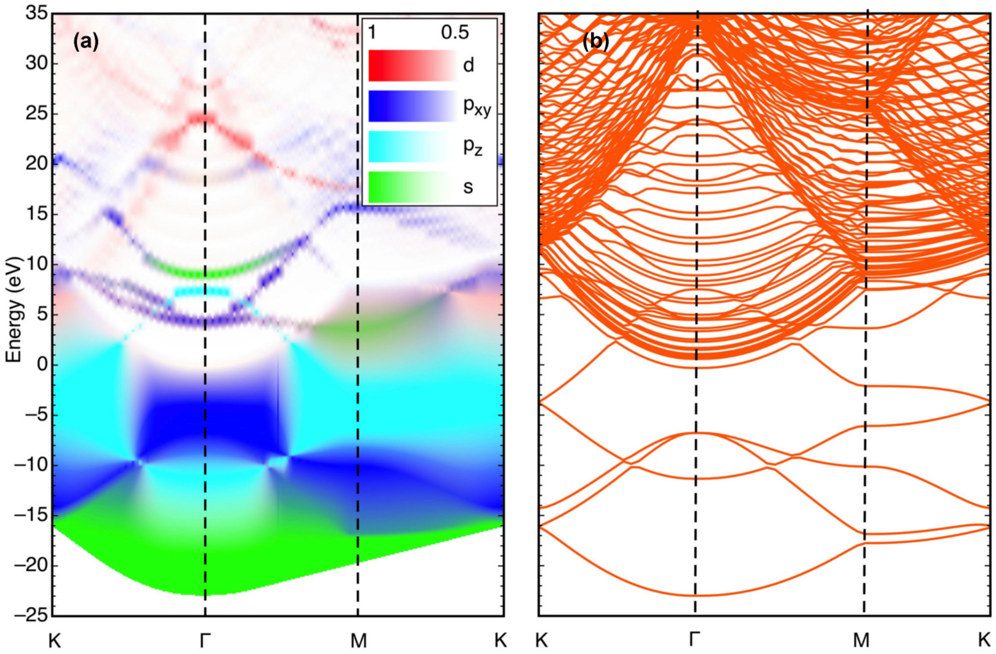

FIG. 5. (Color online) (a) A map illustrating the atomic character of all states in the Brillouin zone. Only states with an atomic character of 50% or higher are shown. All states in the valence band show high atomic character whereas the conduction band consists of an "island" of states with a high atomic character. (b) The graphene band structure along the high-symmetry lines.

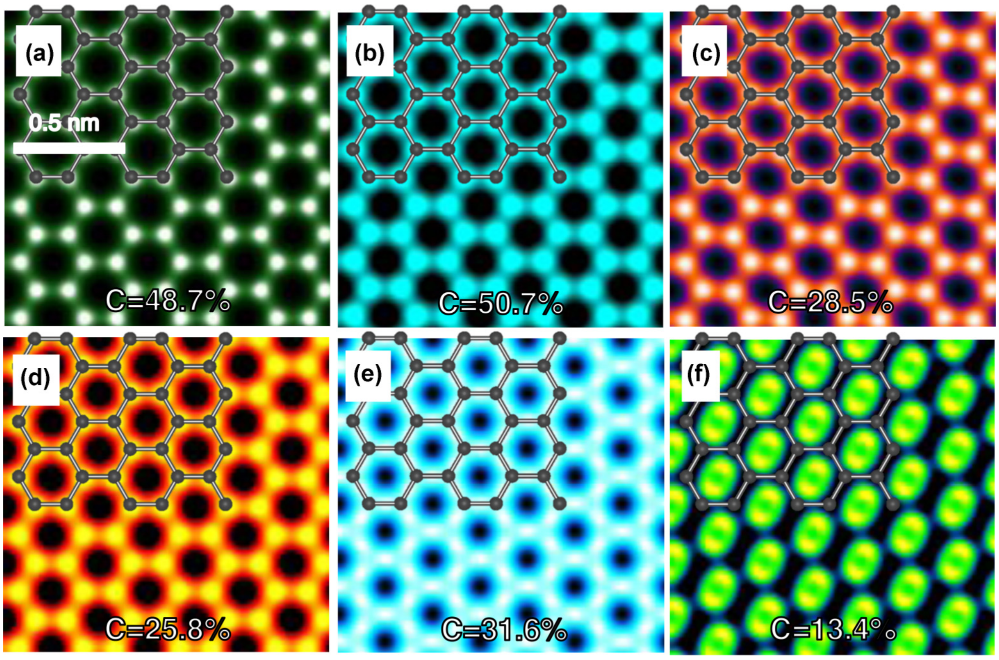

FIG. 6. (Color online) Characteristic images at the Γ point created by non-dipole-allowed (a–c) and dipole-allowed excitations (d–f). (a) s to s excitations; (b) p_z to p_z excitations; (c) p_{xy} to p_{xy} excitations; (d) p_{xy} to s excitation; (e) p_z to d excitations; (f) s to p_{xy} excitations. (d–f) Images show the highest intensity and thus contribute the most to the total image.

less localized on the C atom sites than the p_z to p_z excitations in Fig. 6(b). In particular, the s to p_{xy} transitions in Fig. 6(f) show atomic resolution with reversed contrast, their maxima not coming from the carbon sites. Such contributions lower the overall spectroscopic image contrast.

Using the transitions shown in Figs. 6(a) and 6(f) as an example, we examine the underlying mechanisms resulting in the simulated image contrast. Figure 7(a) reproduces the image Fig. 6(a) while Figs. 7(e) and 7(i) contribute equally to the formation of the delocalized image Fig. 6(f) which

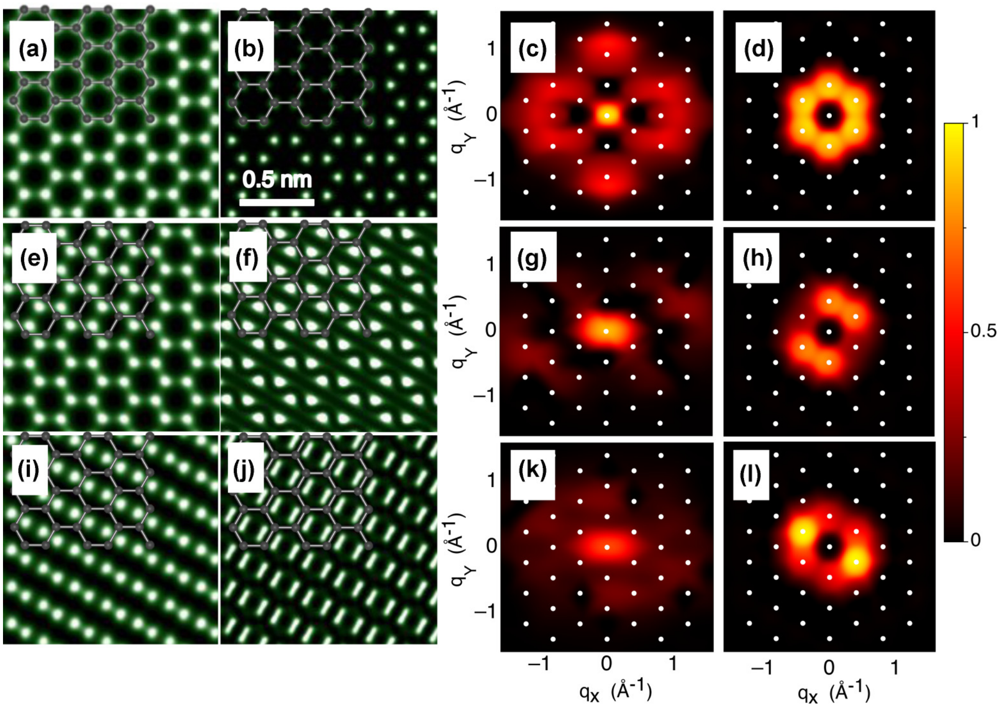

FIG. 7. (Color online) (a) The image of Fig. 6(a). Panels (e, i) contribute equally to the formation of the delocalized image (f) of Fig. 6. Panels (b, f, j) are the inelastic scattering potentials that after convoluting with the probe produce the images (a, e, i), respectively. Panels (c, g, k) are the Fourier transform of (b, f, j), respectively. Panels (d, h, l) are the projected transition matrix elements for each case.

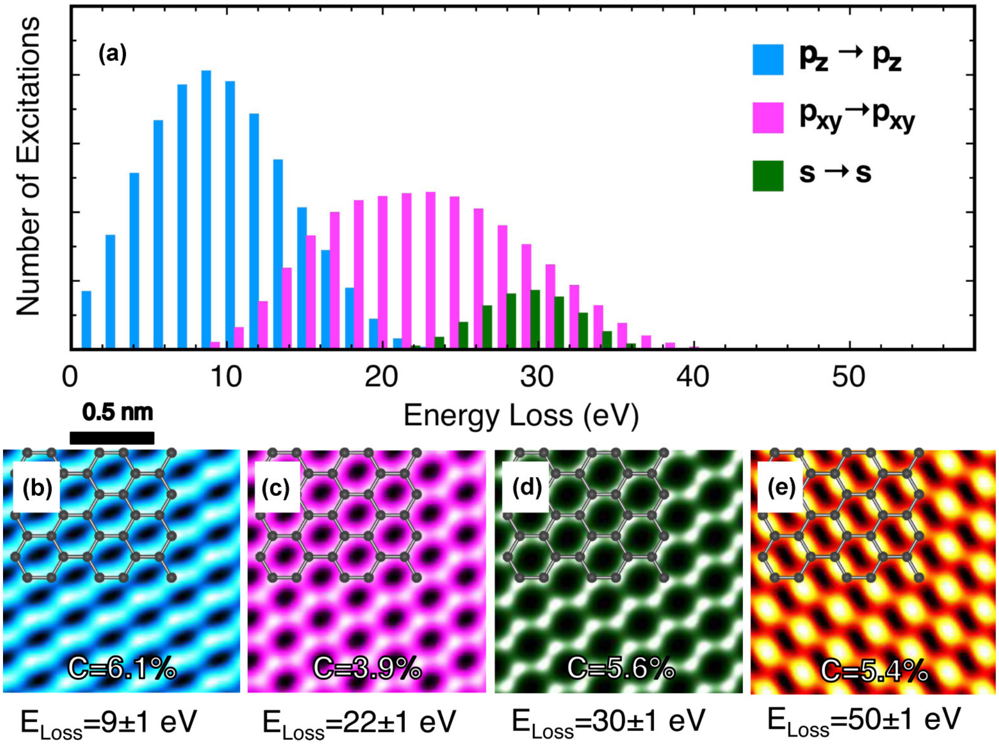

E_{Loss}=9±1 eV E_{Loss}=22±1 eV E_{Loss}=30±1 eV E_{Loss}=50±1 eV

FIG. 8. (Color online) (a) The number of characteristic nondipole excitations as a function of energy loss. (b–e) Images obtained by excitations within the illustrated energy ranges color coded to represent the dominant atomic transition.

comes from excitations to a twofold degenerate p_{xy} state. These images are formed by convolution of the probe intensity with the inelastic scattering potentials shown in Figs. 7(b), 7(f), and 7(j), respectively, as discussed in Sec. II A. While Fig. 7(b) is highly localized on the atomic sites, Figs. 7(f) and 7(j) show intensity inside the graphene ring albeit with two localized features. This is reflected in the Fourier transform of Figs. 7(b), 7(f), and 7(j) shown in Figs. 7(c), 7(g), and 7(k), respectively. Figure 7(c) shows significant intensity at large q values corresponding to localized features in the potential. Figures 7(g) and 7(k) are dominated by low-q features resulting in a less localized potential with a higher background. Figures 7(d), 7(h), and 7(l) show the projected transition matrix elements, given by Eq. (6), for each case. Figure 7(d) indicates a high contribution from transitions with significant transverse momentum transfer. This is reduced in Figs. 7(h) and 7(l) except for two lobes corresponding to the two localized features in Figs. 7(f) and 7(e). It is clear from Fig. 7 that electrons scatter only with momentum transfer smaller than $1\,\text{Å}^{-1}$, which is consistent with the fact that the experimental spectra do not change with the size of the collection apertures used in the experiment (see Sec. II).

The atomic character of the states decreases away from the Γ point in the BZ as shown in Fig. 5. Figure 8(a) shows the joint density of the nondipole excitations including all k points of the BZ. Due to momentum transfer, which is always present in VEELS, the joint density includes also indirect excitations. It is clear that the character of the excitations varies as a function of the energy loss. Excitations with a p_z character (blue) are found mostly at lower energy losses, while the p_{xy} and s excitations are located within the $10-40\,\text{eV}$ range. At higher energies the graphene band structure mostly consists of delocalized d states with a weak atomic character. In order to associate the resulting images with the character of the excitations we calculate images within 2-eV energy windows where the atomic character is maximized. The obtained images are shown in Figs. 8(b)–8(d). It is clear that the contrast of these images is significantly reduced compared to Fig. 6, much closer to that observed experimentally. Figure 8(e) shows an image in which the intensity is not localized at individual atomic sites, but blurs two atomic sites together, consistent with Fig. 2(e). The results confirm that the origin of the experimental contrast lies in these atomiclike transitions. Finally, for energy losses around 50 eV, as in Fig. 8(e), we obtain a low-intensity image, as compared to the rest of the images, with low contrast at the carbon sites. This is due to the lack of highly localized excitations for energies higher than 40 eV. Any atomic contrast within that energy range originates from excitations to states with a weak d character. We thus conclude that the graphenelike images are mostly controlled by excitations that are highly localized. The lower contrast seen experimentally is due to contributions from dipole excitations showing weaker or reversed contrast.

The character of a VEELS image depends strongly on the energy loss integration window. As we show in Fig. 9 by shifting the energy range by a few eVs we obtain images with various patterns. The images in Figs. 9(b)–9(d) show the strong dependence on the energy loss. The lower-energy image (b) shows every other carbon atom bright, which is reversed at the higher-energy range (d). At the 30 eV image we observe again the graphene structure with a comparatively high contrast of 5.3%. The latter is a direct indication that the total image at $26-42\,\text{eV}$ mainly originates by the excitations that are

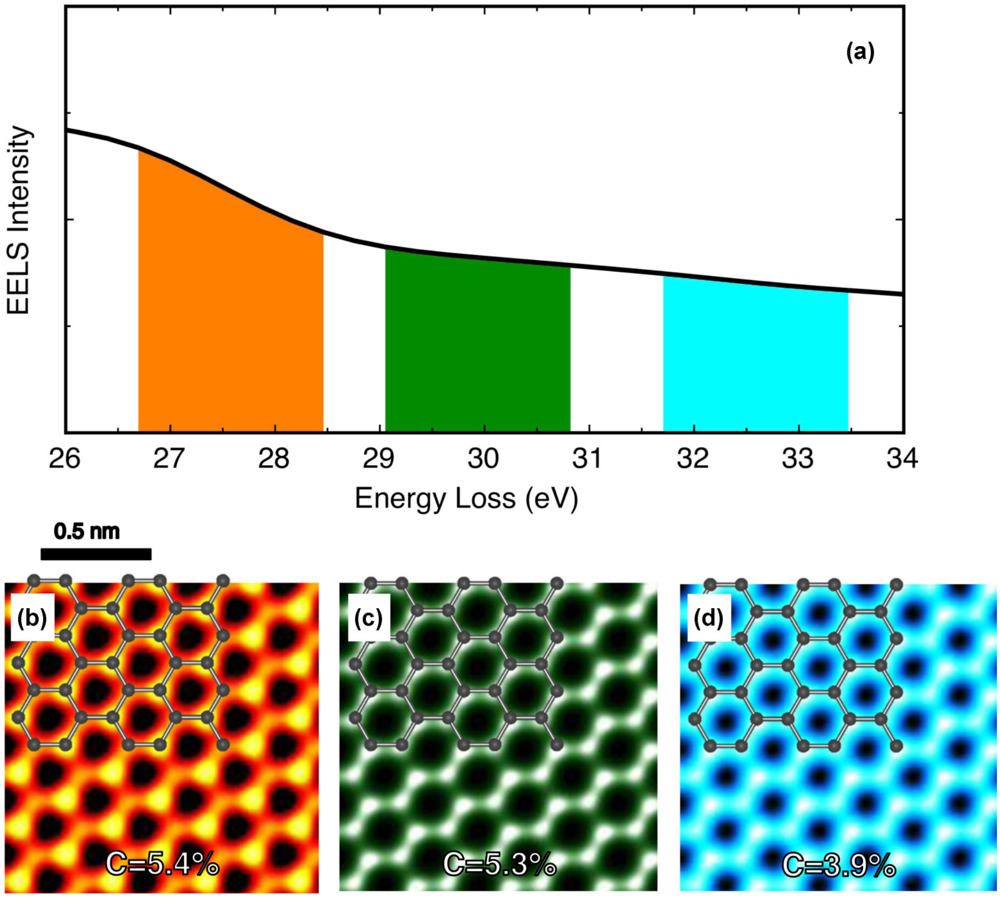

FIG. 9. (Color online) (a) The three highlighted areas where the images in (b–d) are calculated. (b–d) The integrated images obtained within the three highlighted areas in (a) with a 2-eV energy window.

located within a narrow window at around 30 eV. This result is due to interplay between the different types of excitations that coexist within the intermediate energy range. Increased signal-to-noise ratios will open the possibility of experimental measurement from reduced energy windows allowing the exploration of such transitions.

We note further that some of the images in Fig. 8 exhibit the full graphene lattice and others do not. We expect s-s and p_z-p_z transitions to exhibit the full graphene lattice because s and p_z orbitals have the full point-group symmetry of the lattice. This feature is evident in Fig. 6 where we plotted single excitations. In contrast, p_x and p_y orbitals do not have the full point-group symmetry (graphene does not have 90° rotation symmetry). As a result, some of the images in Fig. 8, depending on the energy range, do not exhibit the graphene lattice.

It is clear from Fig. 8(d) that the graphenelike image is directly associated with the existence of s to s excitations within the $29-31$ eV window. The states involved in such excitations have the point-group symmetry of graphene and therefore yield an image that resembles a graphene lattice. On the other hand, images that come from p_z excitations at $8-10$ eV, Fig. 8(b), and p_{xy} excitations at $20-22$ eV, Fig. 8(c), show a rather distorted graphenelike pattern since one spot is much brighter than the other. To understand that feature, one must consider that states with p_{xy} character are degenerate at the Γ point. The one-to-one mixing of the p_x and p_y orbitals at the high symmetry BZ points results in the graphenelike image of Fig. 3(c). However, if we split the image into partial ones, we see that those coming from pairs of states within the subspace exhibit spatial distortions due to the variant p_x-p_y mixing

To demonstrate the effect of degeneracy on the formation of VEELS images we show in Fig. 10 the partial images that contribute equally to the total image in Fig. 6(c), which comes from a fourfold degenerate p_{xy} excitation at the G point. In Fig. 9(e), we plot the line profiles for the partial images (a–d) (y-axis values are normalized to the maximum value of the total image). Although none of the partial line profiles shows graphenelike behavior the total image restores the correct profile. The variant spatial dependence of the partial images is due to different p_x-p_y mixing. Only the total image has a $50\%-50\%$ mixing between p_x and p_y and hence conserves the graphene symmetry. In the general case—where excitations between all k points of the BZ are included—the excitation of a single partial image is now attainable due to the breaking of the degeneracy. Therefore excitations between p_{xy} states do not contribute to the graphenelike images but introduce deviations from the hexagonal pattern.

Such distortions affect images only at k points away from the high-symmetry points where the degeneracy of the p_{xy} orbital is broken. Therefore, the high concentration of p_{xy} excitations around 20 eV is responsible for the distorted graphene

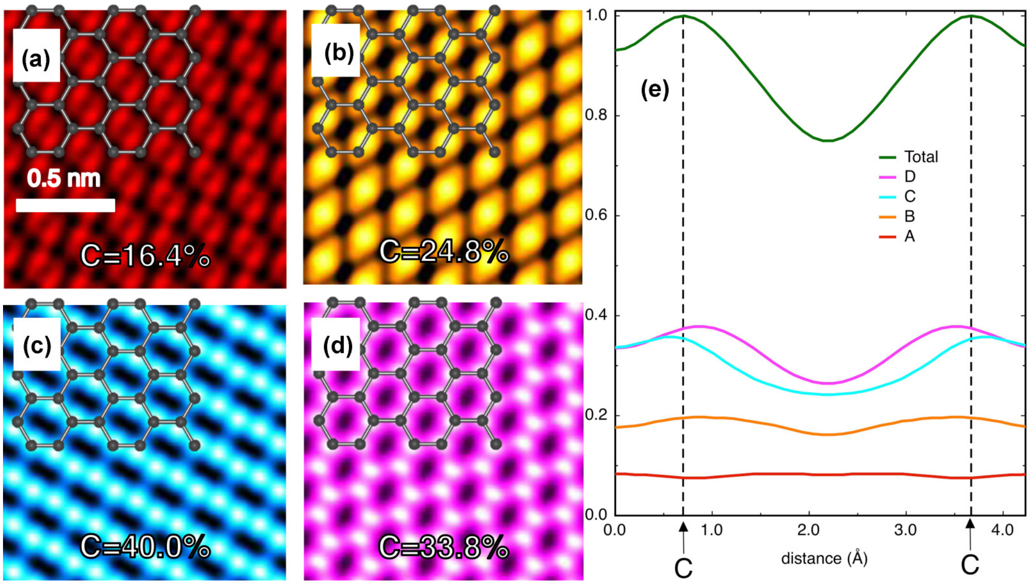

FIG. 10. (Color online) (a–d) Partial images that contribute to the total image in Fig. 6(c). (e) Line profiles for the partial images (a–d) (y-axis values are normalized to the maximum value of the total image).

images calculated theoretically. Although at lower energies the concentration of p_z excitations is higher, the images are still distorted due to strong contributions that come from the remaining p_{xy} excitations. Such contributions are negligible at much lower energies—about 5 eV—and the graphenelike pattern is restored. The latter is clearly demonstrated in Fig. 11 where VEELS images in the two main peaks of the EEL spectrum, namely, the π and $\pi + \sigma$ peaks, are shown. Both images display very low contrast while only the π peak image exhibits a graphenelike structure. According to Fig. 8 the π peak lies within the areas where the p_z excitations are dominant while for the $\pi + \sigma$ peak the p_{xy} excitations contribute in an equal footing. Because of that the image that corresponds to the π peak is graphenelike while the $\pi + \sigma$ peak gives a distorted image.

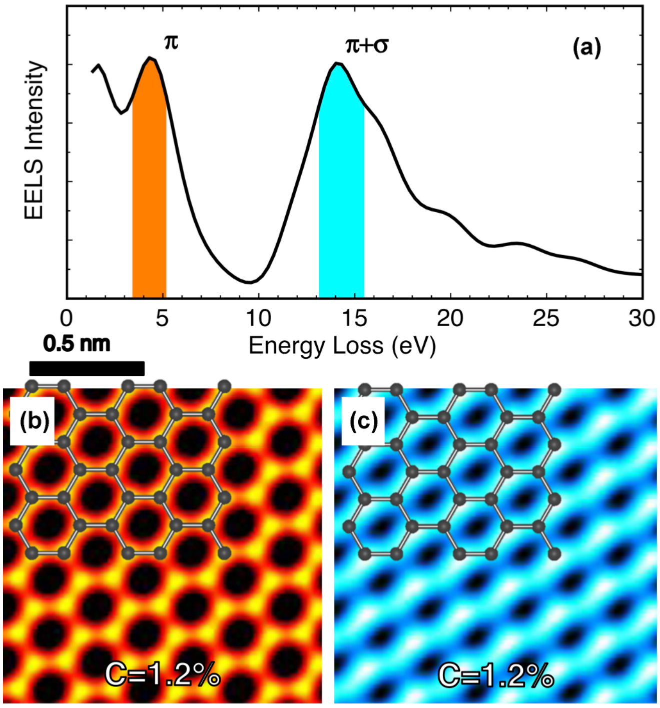

FIG. 11. (Color online) (a) Highlighted areas of the energy ranges for the images in (b, c).

V. CONCLUSIONS

In summary, we have introduced a powerful experimental and theoretical methodology that probes low-energy excitations in solids and nanostructures with atomic resolution, complementing optical spectroscopies that have limited spatial resolution. We demonstrated that certain electron-beam–induced valence-electron excitations contain atomic-scale information that can be revealed by suitable STEM-VEELS maps. We developed a theoretical scheme that allows the direct simulation of such maps. This scheme further allows us to investigate the contributions of individual excitations to the observed features and identify their spatial and orbital characteristics. In this implementation of the technique we chose pristine graphene for computational efficiency, but also because it provides unambiguous evidence for the atomic-scale contrast even in the absence of defects, which naturally induce localization of electronic states. Experimentally, it may be possible to maximize the contribution of the nondipole transitions using special detection schemes such as annular apertures [35].

Though for a perfect crystal the theoretical VEEL maps only provide information about the origin of the transitions that correspond to experimental maps, the technique presented here provides a useful tool for investigating the properties of structural defects and impurities. More specifically, one would be able to compare the experimental maps with theoretical maps corresponding to different atomic configurations and determine which configurations fit the data best. As detectors with improved signal-to-noise ratios and monochromators with higher-energy resolution become available, these alternative atomic-resolution maps may be able to probe all types of low-energy excitations, including plasmons, interband transitions, and phonons. Mapping their variation around defects and interfaces will give fundamental insights into the atomic-scale origins of electronic, magnetic, transport, and thermal properties and provide characteristic signatures for defect identification, offering guidance for atomic-level defect engineering for improved functionality.

ACKNOWLEDGMENTS

This research was supported by DOE Grant No. DE-FG02-09ER46554 (M.D.K., M.P.O., M.P.P., S.T.P.), the Center for Nanophase Materials Sciences (CNMS), which is sponsored at ORNL by the Scientific User Facilities Division, Office of Basic Energy Sciences, U.S. DOE (J.C.I.), by a Wigner Fellowship through the Laboratory Directed Research and Development Program of Oak Ridge National Laboratory (ORNL), managed by UT-Battelle, LLC, for the U.S. DOE (W.Z.), by National Science Foundation through Grant No. DMR-0938330 (W.Z.), and by the Office of Basic Energy Sciences, Materials Sciences and Engineering Division, U.S. DOE (J.L., S.J.P.). Numerical calculations were performed at the Oak Ridge Leadership Computing Facility (OLCF) at Oak Ridge National Laboratory (ORNL) and the National Energy Research Scientific Computing Center (NERSC), which are supported by the Office of Science of the U.S. Department of Energy under Contracts No. DE-AC05-00OR22725 and No. DE-AC02-05CH11231, respectively.

APPENDIX A: PROBE WAVE FUNCTION

In this Appendix we discuss the properties of the fast electron probe as described by a probe wave function. The probe wave function is most easily expressed in reciprocal space as

$$P(\mathbf{R}_0,\mathbf{Q}) = A(\mathbf{Q})\exp[-i\chi(\mathbf{Q})]\exp[-2\pi i\mathbf{Q}\cdot\mathbf{R}_0], \quad \text{(A1)}$$

where the pupil function,

$$A(\mathbf{Q}) = \begin{cases} 1 & \text{for } Q \leqslant Q_{\max} \\ 0 & \text{else} \end{cases}, \quad \text{(A2)}$$

is defined by the probe forming aperture α with $Q_{\max} = k\alpha$ The aberration function is defined as

$$\chi(\mathbf{Q}) = \pi\lambda\Delta f Q^2 + \frac{\pi}{2}\lambda^3 C_s Q^4 + \cdots, \quad \text{(A3)}$$

where λ is the fast electron's wavelength, Δf the probe defocus, and C_s the third-order spherical aberration of the imaging system. We have limited our description to the first aberrations with spherical symmetry. The real-space wave function is simply the inverse Fourier transform of Eq. (A1).

The probe intensity is further modified by incoherence in the imaging system. The simplest is spatial incoherence describing the finite size of the electron source. This can simply be added by convolving the probe intensity with the distribution of the source size. For this work we have assumed a Gaussian source broadening with a full width at half maximum of 0.75 Å. Temporal incoherence is more complicated to deal with in most cases. However, the use of Eq. (A1) allows us to include it directly in the probe intensity. Temporal incoherence is due to the energy spread in the incident electron beam, which due to chromatic aberration of the probe forming optics, leads to a defocus variation δf in the probe. In its simplest form this can be expressed as

$$\delta f = C_c \frac{\Delta E}{E_0}, \quad \text{(A4)}$$

where C_c is the chromatic aberration coefficient, ΔE the energy spread of the incident beam, and E_o the incident energy. For the Nion UltraSTEM 100 used in these results $C_c = 1.33$ mm. The resulting probe intensity is easily calculated as an incoherent sum of probe intensities for different defocus values,

$$|P(\mathbf{R}_0,\mathbf{R})|^2 = \sum_{\delta f} w_{\delta f}|P(\mathbf{R}_0,\mathbf{R},\delta f)|^2, \quad \text{(A5)}$$

where $w_{\delta f}$ is a weighting factor depending on the geometry of the energy/defocus spread.

APPENDIX B: CALCULATION OF THE INELASTIC TRANSITION MATRIX ELEMENT WITHIN THE PAW METHOD

In this Appendix we present the calculation of the matrix elements between an initial electronic state in the valence band and a final state F in the conduction band of the operator $e^{-2\pi i\mathbf{q}\cdot\mathbf{r}}$ given by

$$\langle\Psi_F(\mathbf{r})|e^{-2\pi i\mathbf{q}\cdot\mathbf{r}}|\Psi_I(\mathbf{r})\rangle. \quad \text{(B1)}$$

Both wave functions are given by the following generic formula:

$$\Psi_N(\mathbf{r}) = \tilde{\Psi}_N(\mathbf{r}) + \sum_\alpha [\phi_\alpha(\mathbf{r}) - \tilde{\phi}_\alpha(\mathbf{r})]\langle p_\alpha|\tilde{\Psi}_N\rangle, \quad \text{(B2)}$$

within the formalism of the projector augmented wave method (PAW) [33,34]. The first term of the right-hand side corresponds to the pseudo-wave-function, which is expressed as a plane-wave expansion $\tilde{\Psi}_N(\mathbf{r}) = \sum_{\mathbf{G}} C_N^{\mathbf{G}} e^{2\pi i(\mathbf{G}+\mathbf{k})\cdot\mathbf{r}}$ over the reciprocal vectors $\mathbf{G}$. Note that the pseudo-wave-function is rapidly varying around the core positions in order to be orthogonal to the core states. That makes the accurate description of the electronic states numerically challenging. Moreover the pseudo-wave-functions do not by definition satisfy the orthogonality condition for the higher-energy states of the conduction band. Therefore in order to avoid any unnatural divergence at the low momentum transfer limit it is essential to include the PAW corrections to the electronic wave functions as described by the second term in the right-hand side of Eq. (B2). In this way we obtain a smooth wave function around the cores and simultaneously we ensure the orthogonality and thus the numerical accuracy of our simulations. Note that the index a in Eq. (B2) stands for the atomic quantum numbers nlm and the atomic positions. Also $\phi_i(\mathbf{r}),\tilde{\phi}_i(\mathbf{r})$ are the all-electron (AE) and pseudo (PS) atomic wave functions, which are proportional to a spherical harmonic with a radial weighting $\phi_i(\mathbf{r}) = \Phi_{nl}(r_i)Y_{lm}(\theta,\phi)$ and $\tilde{\phi}_i(\mathbf{r}) = \tilde{\Phi}_{nl}(r_i)Y_{lm}(\theta,\phi)$. The term $\langle p_\alpha|\tilde{\Psi}_N\rangle$ expresses a projection that transforms the AE wave function onto the PS wave function within the sphere with the atomic radius R_c. Moreover, the AE and PS atomic orbitals are constructed in a way to match each other outside of the augmentation sphere, with radius R_{AUG}, which is smaller than the atomic radius R_c.

By substituting the PAW wave function in Eq. (B1) we obtain that the transition matrix element within the PAW formalism is given by

$$\begin{aligned}\langle\Psi_F(\mathbf{r})|e^{-2\pi i\mathbf{q}\cdot\mathbf{r}}|\Psi_I(\mathbf{r})\rangle\\ &= \langle\tilde{\Psi}_F(\mathbf{r})|e^{-2\pi i\mathbf{q}\cdot\mathbf{r}}|\tilde{\Psi}_I(\mathbf{r})\rangle + \sum_{\alpha\beta}\langle\tilde{\Psi}_I \mid p_\alpha\rangle[\langle\phi_\alpha|e^{-2\pi i\mathbf{q}\cdot\mathbf{r}}|\phi_\beta\rangle\\ &\quad - \langle\tilde{\phi}_\alpha|e^{-2\pi i\mathbf{q}\cdot\mathbf{r}}|\tilde{\phi}_\beta\rangle]\langle p_\beta \mid \tilde{\Psi}_F\rangle,\end{aligned} \tag{B3}$$

where we make use the completeness relation $\sum_\alpha |\tilde{\phi}_\alpha\rangle\langle p_\alpha| = 1$ for the projector operators. Although the set of projector operators is complete for an infinite number of projectors, for computational reasons we keep only two projectors for every atomic level lm. Note that for $\boldsymbol{q} = 0$ the above relation is reduced to the orthonormalization relation for the AE wave function,

$$\begin{aligned}\langle\tilde{\psi}_F(\mathbf{r})|\tilde{\psi}_I(\mathbf{r})\rangle + \sum_{\alpha\beta}\langle\tilde{\psi}_I|P_\alpha\rangle[\langle\phi_\alpha|\phi_\beta\rangle - \langle\tilde{\phi}_\alpha|\tilde{\phi}_\beta\rangle]\langle P_\beta|\tilde{\psi}_F\rangle\\ = \delta_{IF}.\end{aligned} \tag{B4}$$

For the calculation of the first part, the matrix elements between the pseudo-wave-functions as in Eq. (B3), we use the form of the plane-wave expansion for the wave function. In this way we found that

$$\begin{aligned}&\langle\tilde{\Psi}_F(\mathbf{r})|e^{-2\pi i\mathbf{q}\cdot\mathbf{r}}|\tilde{\Psi}_I(\mathbf{r})\rangle\\ &\quad = \sum_{\mathbf{G}\mathbf{G}'} C_I^{\mathbf{G}*} C_F^{\mathbf{G}'}\delta(\mathbf{q}+\mathbf{k}+\mathbf{G}-\mathbf{k}'-\mathbf{G}').\end{aligned} \tag{B5}$$

The contribution of the plane-wave expansion to the matrix element has the form of a double sum over the reciprocal vectors G,G′ The pair of these vectors has to satisfy the delta function, which connects the momentum transfer vector $\mathbf{q}$ with the wave vectors $\mathbf{K}$ and $\mathbf{K}'$ of the initial and final state, correspondingly. In this way crystal local-field corrections, which play a crucial role to highly anisotropic 2D materials such as graphene, are taken into account [36].

In order to evaluate numerically the PAW part of the transition matrix element we make use of the expansion

$$e^{-i\mathbf{q}\cdot\mathbf{r}} = 4\pi\sum_{\mathrm{LM}} i^L j_L(qr) Y^*_{\mathrm{LM}}(\hat{\mathbf{q}}) Y_{\mathrm{LM}}(\hat{\mathbf{r}}), \tag{B6}$$

where $j_{\mathrm{L}}(qr)$ is a spherical Bessel function of the first kind, into the PAW part of Eq. (B3), taking into account the fact that the atomic orbitals do not overlap with those on the neighboring site. In this way we found that the PAW part of the matrix element is

$$\begin{aligned}&\langle\Psi_F(\mathbf{r})|e^{-2\pi i\mathbf{q}\cdot\mathbf{r}}|\Psi_I(\mathbf{r})\rangle|_{\mathrm{PAW}}\\ &\quad = \sum_{\alpha\mathrm{LM}}\langle\tilde{\Psi}_I \mid p_\alpha\rangle\langle p_\beta \mid \tilde{\Psi}_F\rangle F^{\mathrm{LM}}_{\alpha\beta} R_{\alpha\beta}(q),\end{aligned} \tag{B7}$$

where we introduce the radial $R^L_{\alpha\beta}(q)$ and the angular $F^{\mathrm{LM}}_{\alpha\beta}$ integrals given by the following formulas:

$$\begin{aligned}R_{\alpha\beta}(q) &= \int_0^{R_C}[\Phi_\alpha(r)\Phi_\beta(r) - \tilde{\Phi}_\alpha(r)\tilde{\Phi}_\beta(r)]j_L(qr)r^2dr,\\ F^{\mathrm{LM}}_{\alpha\beta} &= \int Y^*_\alpha(\hat{r})Y_{\mathrm{LM}}(\hat{r})Y_\beta(\hat{r})d\Omega.\end{aligned} \tag{B8}$$

While the radial integral $R^L_{\alpha\beta}(q)$ needs to be evaluated numerically, the angular integral is written as

$$\begin{aligned}F^{\mathrm{LM}}_{\alpha\beta} &= (-1)^{M_\alpha}\sqrt{\frac{(2L_\alpha+1)(2L+1)(2L_\beta+1)}{4\pi}}\\ &\quad\times\begin{pmatrix} L_\alpha & L_\beta & L\\ -M_\alpha & M_\beta & M\end{pmatrix}\begin{pmatrix} L_\alpha & L_\beta & L\\ 0 & 0 & 0\end{pmatrix},\end{aligned} \tag{B9}$$

where we make use of the properties of the spherical harmonics and the $3j$ symbols. While the angular integral in Eq. (B9) introduces a set of selection rules for the angular momentum the radial integral governs the intensity of the transition matrix element with respect to the momentum transfer.

APPENDIX C: FIRST-PRINCIPLES CALCULATIONS OF THE ELECTRONIC WAVE FUNCTIONS

The initial and final electronic wave functions are calculated within density functional theory (DFT). We carry out the DFT calculations by using the Vienna *ab initio* Simulations Package (VASP) [37–39]. In order to correctly model the vacuum on either side of a graphene sheet we use a two-atom unit cell with a significantly increased size, about 30 Å, along the perpendicular direction. That increases the number of transitions significantly and makes the numerical simulation challenging. In order to converge the density of states and the electronic wave functions up to 60 eV, we use 260 bands and a dense sampling of the Brillouin zone (BZ) with 12×12 k points on the x-y plane. We also work within the local density approximation (LDA) while we take into account the PAW corrections which are essential for the proper treatment of the low-momentum-transfer limit (dipole approximation) [37,40].

---

[1] F. De Angelis, G. Das, P. Candeloro, M. Patrini, M. Galli, A. Bek, M. Lazzarino, I. Maksymov, C. Liberale, L. C. Andreani, and E. Di Fabrizio, Nat. Nanotechnol. **5**, 67 (2010).

[2] W. A. Murray and W. L. Barnes, Adv. Mater. **19**, 3771 (2007).

[3] S. J. Pennycook, Ann Rev Mater. Sci. **22**, 171 (1992).

[4] P. E. Batson, N. Dellby, and O. L. Krivanek, Nature **418**, 617 (2002).

[5] H. Sawada, F. Hosokawa, T. Kaneyama, T. Ishizawa, M. Terao, M. Kawazoe, T. Sannomiya, T. Tomita, Y. Kondo, T. Tanaka, Y. Oshima, Y. Tanishiro, N. Yamamoto, and K. Takayanagi, Jpn. J. Appl. Phys. **46**, L568 (2007).

[6] M. Varela, M. P. Oxley, W. Luo, J. Tao, M. Watanabe, A. R. Lupini, S. T. Pantelides, and S. J. Pennycook, Phys. Rev. B **79**, 085117 (2009).

[7] R. Erni, M. D. Rossell, C. Kisielowski, and U. Dahmen, Phys. Rev Lett. **102**, 096101 (2009).

[8] K. Suenaga, Nat. Chem. **1**, 415 (2009).

[9] O. L. Krivanek, M. F. Chisholm, V. Nicolosi, T. J. Pennycook, G. J. Corbin, N. Dellby, M. F. Murfitt, C. S. Own, Z. S. Szilagyi, M. P. Oxley, S. T. Pantelides, and S. J. Pennycook, Nature **464**, 571 (2010).

[10] W. Zhou, M. P. Oxley, A. R. Lupini, O. L. Krivanek, S. J. Pennycook, and J. C. Idrobo, Microsc. Microanal. **18**, 1342 (2012).

[11] M. P. Prange, M. P. Oxley, M. Varela, S. J. Pennycook, and S. T. Pantelides, Phys Rev. Lett. **109**, 246101 (2012).

[12] M. Bosman, V. J. Keast, J. L. García-Muñoz, A. J. D'Alfonso, S. D. Findlay, and L. J. Allen, Phys Rev. Lett. **99**, 086102 (2007).

[13] D. A. Muller, Science **319**, 1073 (2008).

[14] M. P. Oxley, M. Varela, T. J. Pennycook, K. van Benthem, S. D. Findlay, A. J. D'Alfonso, L. J. Allen, and S. J. Pennycook, Phys. Rev. B **76**, 064303 (2007).

[15] K. Suenaga, M. Tencé, C. Mory, C. Colliex, H. Kato, T. Okazaki, H. Shinohara, K. Hirahara, S. Bandow, and S. Iijima, Science **290**, 2280 (2000).

[16] M. Varela, S. D. Findlay, A. R. Lupini, H. M. Christen, A. Y. Borisevich, N. Dellby, O. L. Krivanek, P. D. Nellist, M. P. Oxley, L. J. Allen, and S. J. Pennycook, Phys. Rev. Lett. **92**, 095502 (2004).

[17] M. P. Oxley, M. D. Kapetanakis, M. P. Prange, M. Varela, S. J. Pennycook, and S. T. Pantelides, Microsc Microanal. **20**, 784 (2014).

[18] W. Zhou, J. Lee, J. Nanda, S. T. Pantelides, S. J. Pennycook, and J. C. Idrobo, Nat Nanotechnol. **7**, 161 (2012).

[19] A. Y. Borisevich, H. J. Chang, M. Huijben, M. P. Oxley, S. Okamoto, M. K. Niranjan, J. D. Burton, E. Y. Tsymbal, Y. H. Chu, P. Yu, R. Ramesh, S. V. Kalinin, and S. J. Pennycook, Phys Rev. Lett. **105**, 087204 (2010).

[20] W. Zhou, S. J. Pennycook, and J. C. Idrobo, Ultramicroscopy **119**, 51 (2012).

[21] T. W. Josefsson, R. L. Cobal, and L. J. Allen, Phys. Rev. B **54**, 12873 (1996).

[22] J. Verbeeck, D. van Dyck, H. Lichte, P. Potapov, and P. Schattschneider, Ultramicroscopy **102**, 239 (2005).

[23] R. Egoavil, N. Gauquelin, G. T. Martinez, S. Van Aert, G. Van Tendeloo, and J. Verbeeck, Ultramicroscopy **147**, 1 (2014).

[24] K. Van Benthem, R. French, W. Sigle, C. Elsässer, and M. Rühle, Ultramicroscopy **86**, 303 (2001).

[25] R. Egerton, Ultramicroscopy **107**, 575 (2007).

[26] D. Muller and J. Silcox, Ultramicroscopy **59**, 195 (1995).

[27] S. L. Cundy, A. Howie, and U. Valdrè, Philos. Mag. **20**, 147 (1969).

[28] T. Yamazaki, Y. Kotaka, M. Tsukada, and Y. Kataoka, Ultramicroscopy **110**, 1161 (2010).

[29] H. Kohl and H. Rose, in *Advances in Electronics and Electron Physics*, edited by P. W. Hawkes (Academic Press, New York, 1985), p. 173.

[30] S. D. Findlay, M. P. Oxley, and L. J. Allen, Microsc. Microanal. **14**, 48 (2008).

[31] J. M. Cowley and A. F. Moodie, Acta Crystallogr. **10**, 609 (1957).

[32] E. J. Kirkland, *Advanced Computing in Electron Microscopy*, 2nd ed. (Plenum Press, New York and London, 2010).

[33] E. J. Kirkland, R. F. Loane, and J. Silcox, Ultramicroscopy **23**, 77 (1987).

[34] L. Yang, J. Deslippe, C.-H. Park, M. L. Cohen, and S. G. Louie, Phys. Rev. Lett **103**, 186802 (2009).

[35] B. Rafferty and S. J. Pennycook, Ultramicroscopy **78**, 141 (1999).

[36] H.-C. Weissker, J. Serrano, S. Huotari, F. Bruneval, F. Sottile, G. Monaco, M. Krisch, V. Olevano, and L. Reining, Phys. Rev. Lett. **97**, 237602 (2006).

[37] G. Kresse and D. Joubert, Phys. Rev. B **59**, 1758 (1999).

[38] G. Kresse and J. Furthmüller, Phys. Rev. B **54**, 11169 (1996).

[39] G. Kresse and J. Furthmüller, Comput. Mater. Sci. **6**, 15 (1996).

[40] B. Adolph, J. Furthmüller, and F. Bechstedt, Phys. Rev. B **63**, 125108 (2001).